Check for updates

Advanced Materials Technologies

ADVANCED MATERIALS TECHNOLOGIES
www.advmattechnol.com

RESEARCH ARTICLE OPEN ACCESS

Wafer-Scale Top-Down Patterning of Metal Halide Perovskites

Federico Fabrizi[1,2] | Ardeshir Esteki[2] | Holger Lerch[1] | Saeed Goudarzi[2] | Liudmila Starodubtceva[2] | Gerhard Müller-Newen[3] | Maryam Mohammadi[1] | Max C. Lemme[1,2]

[1]AMO GmbH, Aachen, Germany | [2]Chair of Electronic Devices, RWTH Aachen University, Aachen, Germany | [3]Institute of Biochemistry and Molecular Biology, Uniklinik RWTH Aachen, Aachen, Germany

Correspondence: Maryam Mohammadi (mohammadi@amo.de) | Max C. Lemme (max.lemme@eld.rwth-aachen.de)

Received: 30 June 2026 | **Revised:** 13 September 2026 | **Accepted:** 17 September 2026

Keywords: metal halide perovskite | top-down lithography | wafer scale integration

ABSTRACT

Metal halide perovskites (MHPs) are promising semiconductor materials for next-generation integrated photonics and electronics because they can be deposited from solution at low temperatures, enabling their monolithic integration with conventional semiconductor substrates. However, ionic bonding renders them vulnerable to many standard semiconductor lithography steps involving solvents, developers, or plasma exposure, limiting their integration into standard semiconductor processing. In this work, we demonstrate 150 mm wafer-scale integration of cesium lead bromide ($CsPbBr_3$) MHP thin films using a standard top-down lithographic approach. A chemically amplified resist, polymethyl methacrylate (CAR-PMMA), and a perovskite-compatible developer were employed to enable direct photolithography and pattern transfer via reactive ion etching (RIE). We assessed the structural, optical, and morphological properties of the thin films after patterning via X-ray diffraction, ultraviolet–visible absorption and photoluminescence spectroscopy, and spectroscopic ellipsometry, atomic force microscopy, and electron scanning microscopy, confirming their robustness. Our wafer-scalable approach reduces the need for complex multilayer resist stacks, is compatible with i-line stepper lithography for sub-micron device feature sizes, and advances the semiconductor-technology-compatible integration of $CsPbBr_3$-based devices.

1 | Introduction

Metal halide perovskites (MHPs) have emerged as a new class of semiconducting materials with exceptional optoelectronic properties [1, 2]. Their high absorption coefficients [3, 4], tunable bandgaps [1, 5], low exciton binding energies [6, 7], and long carrier diffusion lengths [8, 9] have enabled very promising performance in perovskite solar cells [10]. Their power conversion efficiencies surpass those of silicon-based devices, reaching 34.85% with a perovskite/Silicon configuration. Moreover, their solution processability and low-cost fabrication make MHPs promising materials for a wide range of photonic and electronic devices, including light-emitting diodes (LEDs) [11, 12], photodetectors [13, 14], and lasers [15, 16]. Despite these advantages, integrating MHPs into standard semiconductor fabrication workflows remains challenging [17, 18]. MHPs are intrinsically sensitive to many chemicals involved in conventional semiconductor fabrication processes [19, 20]. This chemical sensitivity can cause MHP degradation and phase instability during patterning. Consequently, most reported MHP devices rely on non-scalable techniques, such as shadow masking [21] and soft lithography [22], which do not provide the precision and reproducibility required for industrial applications. In addition, perovskite-compatible patterning methods, including protective bilayer resist stacks [20], sacrificial layers [23], double-layer transfer printing [24, 25], and cracked-film lithography [24, 25],

This is an open access article under the terms of the Creative Commons Attribution License, which permits use, distribution and reproduction in any medium, provided the original work is properly cited.
© 2026 The Author(s). *Advanced Materials Technologies* published by Wiley-VCH GmbH

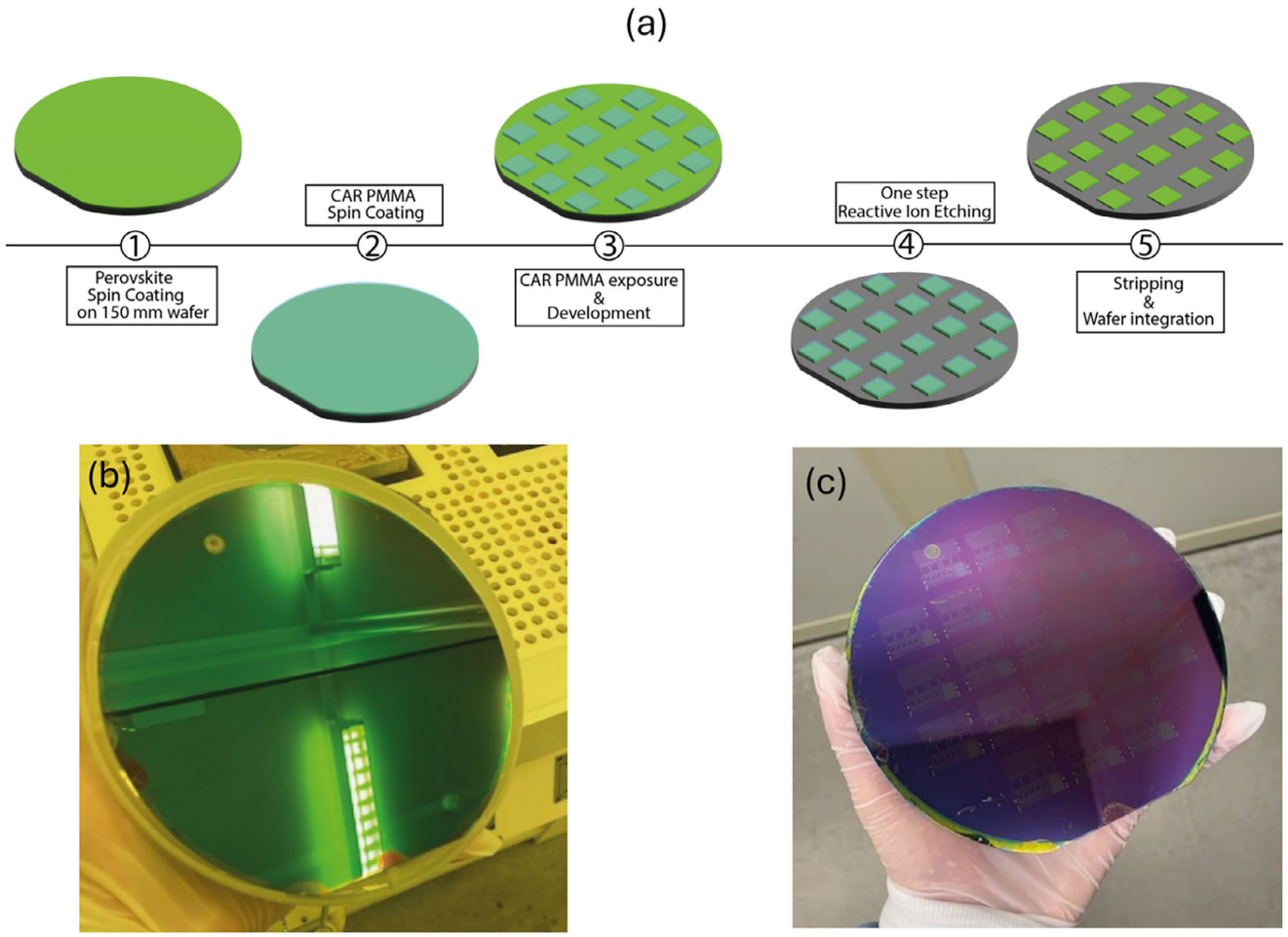


FIGURE 1 | (a) Fabrication process flow of the MHPs wafer-scale integration (consequent steps marked with numbers): (1) deposition of the perovskite thin film on a 150 mm wafer (2) deposition of the CAR-PMMA layer (3) i-line stepper exposure and development (4) pattern transfer into the perovskite layer by one-step reactive ion etching (5) resist stripping in an organic solvent. (b) Representative image of a 150 mm wafer spin-coated with a $CsPbBr_3$ thin film. (c) A Wafer with patterned $CsPbBr_3$ features after reactive ion etching and CAR-PMMA stripping.

have been explored, albeit with increased complexity. To date, direct lithographic patterning of MHPs at the wafer scale has not been demonstrated, although such capability is a prerequisite for the commercialization of perovskite-based integrated photonic and optoelectronic devices. For these applications, a scalable lithographic process needs to combine high spatial resolution and precise alignment with compatibility for multilayer fabrication, while preserving the optical and electronic properties of the perovskite [26, 27]. In this work, we present a simplified wafer-scale integration of cesium lead bromide ($CsPbBr_3$) using a single 300 nm chemically amplified resist, polymethyl methacrylate (CAR-PMMA) combined with i-line stepper lithography, replacing the protective double-resist stack and contact-mask lithography used in our previous work [20]. The i-line stepper (Canon FPA-3000 $i5^+$) provides controlled alignment, overlay, and step-and-repeat exposure across a 150 mm wafer, while the single-resist scheme reduces process complexity and the number of etching cycles. The process enables sub-micron patterning, with resolved structures down to approximately 800 nm, while preserving the optical and structural properties of the material across the wafer. This demonstrates a direct lithography and etching approach for perovskite materials compatible with semiconductor manufacturing.

2 | Results and Discussion

We developed a lithographic workflow compatible with $CsPbBr_3$ thin films for optoelectronic device fabrication (Figure 1a). The process involved spin-coating a $CsPbBr_3$ thin film (Figure S1) onto a Si/SiO_2 150 mm wafer (Figure 1b), followed by deposition of a 300 nm CAR-PMMA layer, UV exposure (i-Line Stepper/Canon-FPA 3000 $i5^+$), and development. CAR-PMMA (AllResist, X AR-N 4800/16) has high sensitivity over the wavelength range of 300–410 nm, enabling direct exposure of 150 mm wafers using an i-line stepper with an excitation wavelength of 365 nm. We used AllResist X AR 300–74/1, a nonpolar organic developer compatible with MHPs. Its compatibility with all-inorganic $CsPbBr_3$ and hybrid organic–inorganic methylammonium lead iodide ($MAPbI_3$) thin films was assessed via optical spectroscopy. Figure S2 shows that their photoluminescence (PL) spectra remained unchanged after 5 min of exposure to the developer. The $CsPbBr_3$ sample was then etched via a PlasmaLab System 100 inductively coupled plasma reactive ion etching (ICP-RIE) tool (Oxford Instruments), and the resist was stripped for 60 min at 80°C in toluene, a nonpolar solvent (see Section 4 for the complete lithography, etching, and stripping conditions) (Figure 1c).

2365709x, 0, Downloaded from https://advanced.onlinelibrary.wiley.com/doi/10.1002/admt.71346 by Universitatsbibliothek RWTH Aachen University, Wiley Online Library on [06/10/2026]. See the Terms and Conditions (https://onlinelibrary.wiley.com/terms-and-conditions) on Wiley Online Library for rules of use; OA articles are governed by the applicable Creative Commons License

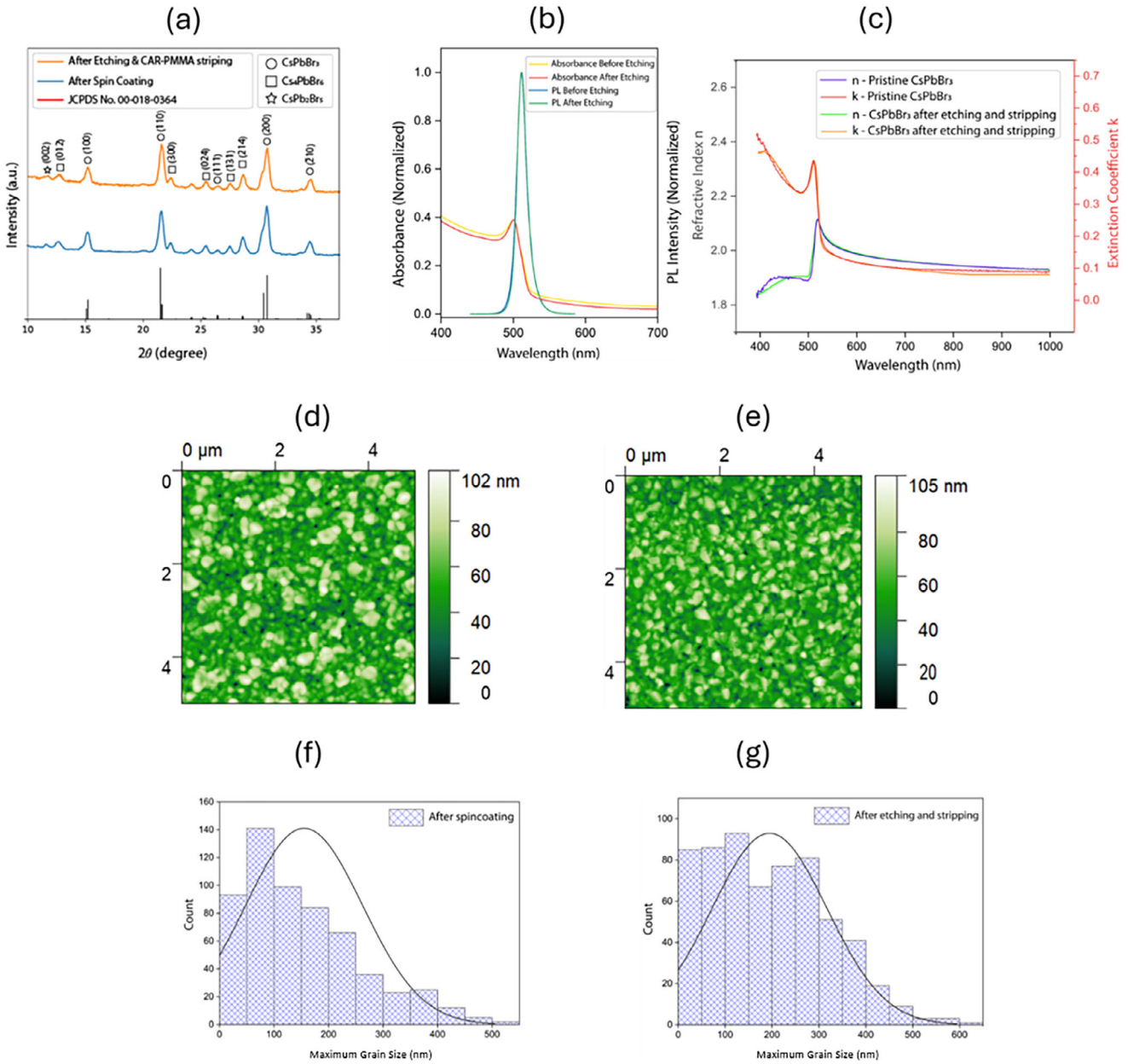


FIGURE 2 | $CsPbBr_3$ morphology and optical characterization. (a) XRD patterns of the samples before and after etching. (b) UV–vis spectra and PL spectra before and after etching. (c) Refractive index (n) and extinction coefficient (k) before and after etching. (d) AFM scan of the $CsPbBr_3$ thin film after wafer-scale spin coating. (e) AFM image of the thin film after etching and stripping of the CAR-PMMA. (f) Grain size analysis of the pristine thin film. (g) Grain size analysis of the thin film after etching and stripping of the resist.

The X-ray diffraction (XRD) patterns before and after etching show distinct high-intensity peaks at 15.21°, 21.49°, 26.37°, 30.69°, 34.46°, and 37.90° (Figure 2a), corresponding to the (100), (110), (111), (200), ($2\bar{1}0$), and ($2\bar{1}1$) crystallographic planes of monoclinic $CsPbBr_3$ (reference code: JCPDS 00-018-0364), respectively [26, 28]. Additional peaks at 12.63°, 22.41°, 25.42°, 27.51°, and 28.63° indicate the presence of the (012), (300), (024), (131), and (214) planes of the rhombohedral Cs_4PbBr_6 phase, respectively [29]. A peak attributed to the (002) plane of the $CsPb_2Br_5$ phase was also observed [30, 31]. The patterned $CsPbBr_3$ was further characterized through ultraviolet–visible (UV-vis) absorption and PL spectroscopy. The absorption edge was approximately 498 nm before and after etching. The PL peak remained at 511.7 nm, with a full width at half maximum (FWHM) of 14.3 nm (Figure 2b). In addition, spectroscopic ellipsometry revealed that the refractive index (n) and extinction coefficient (k) of $CsPbBr_3$ did not change significantly after etching (Figure 2c). Figure 2d,e displays atomic force microscopy (AFM) images of the surface topography of the $CsPbBr_3$ thin film before and after etching. The bright areas with greater heights are attributed to the secondary phases, $CsPb2Br_5$ and Cs_4PbBr_6, as confirmed by XRD (Figure 2a) [32]. The root mean square (RMS) roughness of the spin-coated $CsPbBr_3$ thin film was 14.92 ± 1.57 nm, which decreased slightly to 13.47 ± 1.05 nm after the etching process. This small change is within the measurement scatter, indicating no plasma-induced surface roughening. The average grain size

2365709x, 0, Downloaded from https://advanced.onlinelibrary.wiley.com/doi/10.1002/admt.71346 by Universitatsbibliothek RWTH Aachen University, Wiley Online Library on [06/10/2026]. See the Terms and Conditions (https://onlinelibrary.wiley.com/terms-and-conditions) on Wiley Online Library for rules of use; OA articles are governed by the applicable Creative Commons License

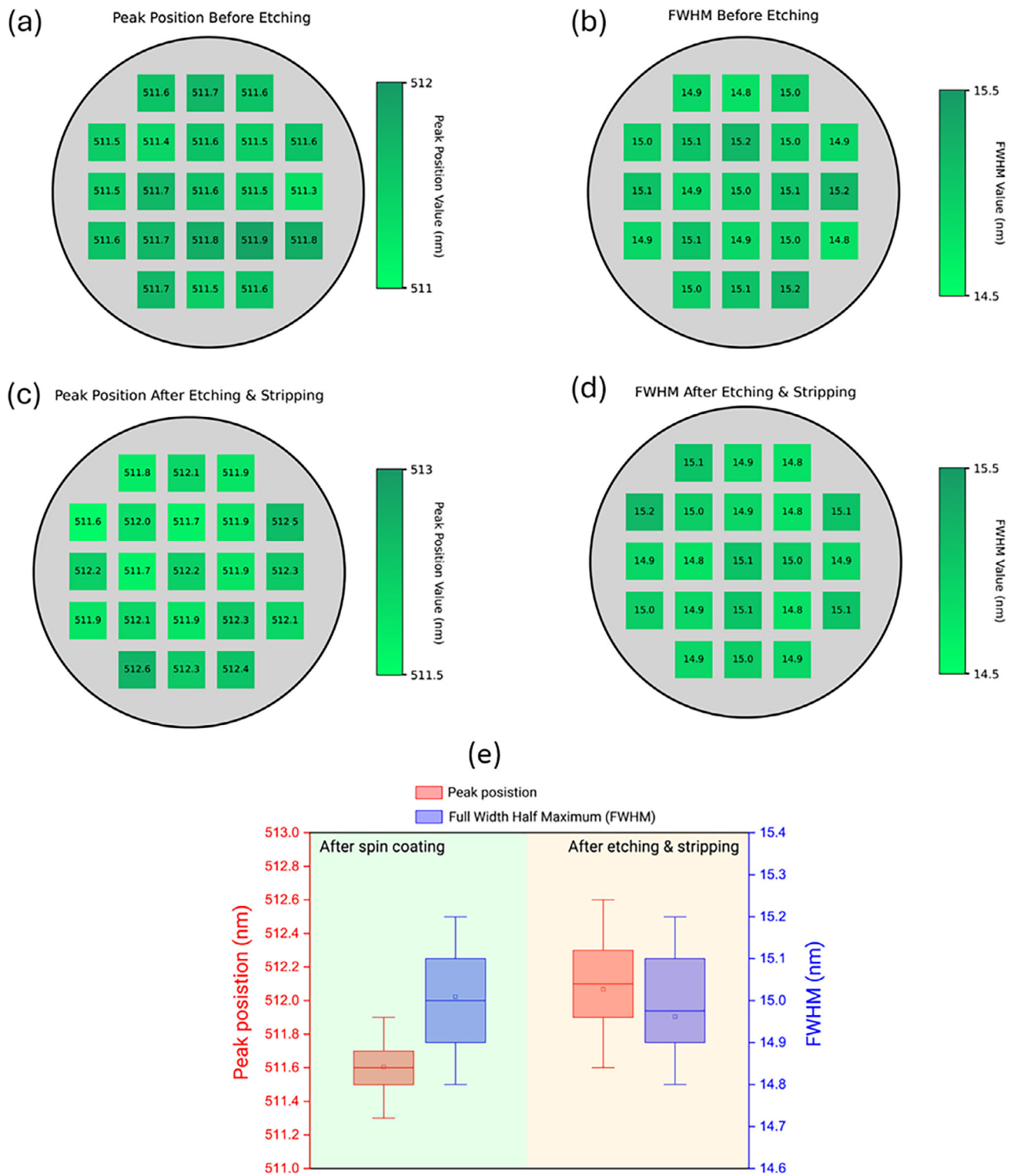


FIGURE 3 | Wafer-scale PL measurements and characterization. (a) Spatial distribution map across the entire wafer of the peak position and (b) FWHM for all 21 dies before the etching process. (c) Spatial distribution map across the entire wafer of the peak position and (d) FWHM for all 21 dies after the etching process and the stripping of the CAR-PMMA. (e) Statistical analysis of the peak position and FWHM across the 21 dies of the wafer.

slightly increased from 156 to 196 nm (Figure 2f,g) after etching and stripping of the PMMA. This observation suggests limited thermally assisted recrystallization during the ICP-RIE process. Process-induced heating can promote grain coalescence and partial conversion of secondary Cs-rich and Pb-rich phases, such as Cs_4PbBr_6 and $CsPb_2Br_5$, into $CsPbBr_3$, thereby increasing the grain size [33–35]. This interpretation is supported by the reduced prominence of the bright secondary-phase-like regions observed in the AFM images after patterning (Figure 2d,e). Compared with our previously reported double-stack photoresist process, in

2365709x, 0, Downloaded from https://advanced.onlinelibrary.wiley.com/doi/10.1002/admt.71346 by Universitatsbibliothek RWTH Aachen University, Wiley Online Library on [06/10/2026]. See the Terms and Conditions (https://onlinelibrary.wiley.com/terms-and-conditions) on Wiley Online Library for rules of use; OA articles are governed by the applicable Creative Commons License

which the grain size increased from approximately 65–200 nm [20], the present process resulted in less grain growth because fewer etching cycles reduced the thermal load during the ICP-RIE process. As a result, all the material characteristics of the $CsPbBr_3$ remained almost constant before and after reactive ion etching.

Wafer-scale patterning is demonstrated in Figure S3, which shows the fully patterned 150 mm wafer together with fluorescence micrographs from representative dies. Diffraction from the periodic device fields is visible across the wafer, while the fluorescence images confirm well-defined patterned structures after etching. Higher-magnification optical microscopy images of selected micropatterns are presented in Figure S4, providing a closer view of the pattern fidelity. Top-view scanning electron microscopy (SEM) further shows a well-defined boundary between the remaining $CsPbBr_3$ film and the exposed SiO_2 substrate, indicating effective removal of the perovskite from the etched region (Figure S5). Cross-sectional SEM of an etched feature (Figure S6a) further confirms complete removal of the perovskite down to the underlying SiO_2, with well-defined sidewalls. The narrowest fully etched feature observed in the cross-sectional images is approximately 800 nm wide (Figure S6b), demonstrating that sub-micron structures are accessible using the present i-line process. Figure S7 presents profilometer line scans after CAR-PMMA development and after ICP-RIE etching and resist stripping, showing a CAR-PMMA thickness of approximately 290 nm and a remaining $CsPbBr_3$ film thickness of approximately 110 nm. The etch depth was further evaluated across 21 dies distributed over the entire wafer. The average thickness was 92.3 nm with a standard deviation of 12.6 nm and exhibited a centre-to-edge gradient of −0.56 nm/mm (Figure S8). Cross-sectional SEM measurements at three radial positions, 115 nm near the center, 80 nm at an intermediate radius, and 70 nm toward the edge (Figure S1), are consistent with this radial trend, supporting the observed spatial variation in etch depth across the wafer.

We evaluated the compatibility of the developed process with a $CsPbBr_3$ thin film across the entire 150 mm wafer using PL spectroscopy before and after etching at 21 dies distributed across the full substrate. Figure 3a,b show wafer-scale maps of the PL peak position and FWHM values measured at predefined points on each die before etching, whereas Figure 3c,d show the corresponding maps after the etching and stripping process. Figure 3e presents the statistical results in a box plot. Figures S9 and S10 show the individual PL spectra recorded for all 21 dies before and after patterning. Before etching, the peak position was 511.6 ± 0.6 nm, with an average FWHM of 15 ± 0.4 nm. After etching and stripping, the peak position shifted slightly to 512.1 ± 1 nm, while the FWHM remained nearly unchanged (14.9 ± 0.4 nm). These results indicate that patterning does not alter the band-edge emission and does not induce spectral broadening [36, 37], supporting the reproducibility and robustness of the patterning process in the $CsPbBr_3$ films. However, steady-state PL peak position and linewidth alone cannot rule out additional non-radiative recombination pathways, such as trap-assisted recombination associated with etching-induced surface and sidewall defects. Future time-resolved photoluminescence (TRPL) measurements could solidify this conclusion.

3 | Conclusions

In this study, we introduced a 150 mm wafer-scale process for top-down patterning of $CsPbBr_3$ films using a CAR-PMMA resist (AllResist, X AR-N 4800/16) and a perovskite-compatible developer (X AR 300–74/1). The process was validated by XRD, UV–vis absorption, PL, and spectroscopic ellipsometry, as well as AFM and SEM, which revealed that the $CsPbBr_3$ films preserved their phase crystallinity, optical, and morphological properties after patterning. The process was demonstrated on an i-line stepper, the workhorse exposure tool of industrial complementary metal–oxide–semiconductor (CMOS)lithography, and cross-sectional SEM confirmed fully etched features down to approximately 800 nm. Wafer-scale uniformity of the optical properties was verified over 21 dies across the full substrate, and multi-wafer reproducibility, along with extension to further perovskite compositions, are the next steps toward manufacturing-level qualification. This represents a significant advance in perovskite electronics and photonics, paving the way for fully scalable and industry-compatible sub-micron device integration of MHPs.

4 | Methods

4.1 | Substrates

The Si/SiO_2 150 mm wafer was cleaned via sonication in acetone and isopropanol, followed by 10 min of oxygen plasma cleaning in an RF plasma reactor. The wafer was then transferred into a nitrogen-filled glove box for perovskite deposition.

4.2 | $CsPbBr_3$ Deposition

$CsPbBr_3$ films were prepared using the precursor formulation reported previously [20]. For wafer-scale coating, 2 mL of solution was dispensed onto the 150 mm substrate and spin-coated at 2000 rpm for 45 s, followed by annealing at 80°C for 10 min.

4.3 | Photolithography

A 300 nm layer of the negative CAR-PMMA (AllResist, X AR-N 4800/16) was spin-coated onto the $CsPbBr_3$ film at 2500 rpm for 45 s and soft-baked at 60°C for 10 min. Exposure was performed on a Canon FPA-3000 $i5^+$ i-line stepper at 365 nm with a dose of 60 mJ cm^{-2}, followed by a post-exposure bake at 60°C for 180 s. The exposed wafers were developed for 180 s at room temperature in the non-polar organic developer X AR 300–74/1 (AllResist).

4.4 | ICP-RIE Etching

Pattern transfer into $CsPbBr_3$ was performed in a PlasmaLab System 100 ICP-RIE system (Oxford Instruments) using an HBr/BCl_3 plasma chemistry, adapted from our earlier etching approach [20]. The measured etch rate was approximately 80 nm min^{-1}, with a selectivity of 3.5 over SiO_2. To minimize process-induced heating, etching was divided into three cycles separated by 2 min cooling periods, which were sufficient to completely remove the exposed perovskite.

2365709x, 0, Downloaded from https://advanced.onlinelibrary.wiley.com/doi/10.1002/admt.71346 by Universitatsbibliothek RWTH Aachen University, Wiley Online Library on [06/10/2026]. See the Terms and Conditions (https://onlinelibrary.wiley.com/terms-and-conditions) on Wiley Online Library for rules of use; OA articles are governed by the applicable Creative Commons License

4.5 | Resist Stripping

The negative CAR-PMMA was removed in toluene at 80°C for 1 h, followed by drying under nitrogen flow.

4.6 | XRD

XRD measurements were performed before and after patterning using a PANalytical diffractometer equipped with filtered Cu Kα radiation ($\lambda = 1.5405$ Å) and operated at 40 kV and 40 mA.

4.7 | UV–vis Absorption Spectroscopy

Absorption spectra of the films before and after patterning were acquired from 300 to 800 nm using a PerkinElmer Lambda 1050 spectrophotometer.

4.8 | Photoluminescence Characterization

PL spectra were acquired at room temperature under ambient conditions using a WITec alpha300R confocal Raman microscope with 457 nm excitation at a laser power of 1 μW. The objective has a numerical aperture of 0.9, corresponding to a diffraction-limited spot diameter of $d = 1.22\lambda/NA \approx 0.6$ μm, which defines the lateral resolution of the PL measurement. Measurements were performed before patterning and after completion of the nanofabrication process. At each die position, 10 spectra were acquired and averaged.

4.9 | Spectroscopic Ellipsometry

Spectroscopic ellipsometry was performed using a J. A. Woollam M-2000 instrument, and the experimental data were analyzed and modelled with CompleteEASE software.

4.10 | AFM and SEM

Surface morphology was examined by tapping-mode AFM using a Bruker Dimension Icon, while SEM imaging was performed with a Zeiss SUPRA 60 operated at 4 kV and a working distance of 3.5 mm.

Acknowledgements

This project has been funded by Deutsche Forschungsgemeinschaft within TRR 404 Active-3D (project numbers 528378584, 441341044), the European Union's Horizon 2020 research and innovation programme under the Marie Skłodowska-Curie grant agreement No. 956270, the German Research Foundation (DFG) through the project Hiper-Lase (GI 1145/4-1 and LE 2440/12-1) and Federal Ministry of Research, Technology, and Space (BMFTR) through the project NEPOMUQ (13N17112). The authors thank P. Grewe and Dr. U. Böttger (Electronic Material Research Lab, RWTH Aachen University) for their support in the XRD measurements. This work was also supported by the Confocal Microscopy Facility, a Core Facility of the Interdisciplinary Center for Clinical Research (IZKF) Aachen within the Faculty of Medicine at RWTH Aachen University.

Open access funding enabled and organized by Projekt DEAL.

Conflicts of Interest

The authors declare no conflicts of interest.

Data Availability Statement

The data that support the findings of this study are available from the corresponding author upon reasonable request.

References

1. J. S. Manser, J. A. Christians, and P. V. Kamat, "Intriguing Optoelectronic Properties of Metal Halide Perovskites," *Chemical Reviews* 116, no. 21 (2016): 12956–13008, https://doi.org/10.1021/acs.chemrev.6b00136.

2. A. J. Olasoji, J. K. Park, H. J. Lee, Y. Song, D. S. Lee, and S. H. Im, "Metal Halide Perovskites: A Platform for next-Generation Multifunctional Devices," *Advances in Industrial and Engineering Chemistry* 1, no. 1 (2025): 12, https://doi.org/10.1007/s44405-025-00011-2.

3. H.-S. Kim, C.-R. Lee, J.-H. Im, et al., "Lead Iodide Perovskite Sensitized all-Solid-State Submicron Thin Film Mesoscopic Solar Cell with Efficiency Exceeding 9%," *Scientific Reports* 2, no. 1 (2012): 591, https://doi.org/10.1038/srep00591.

4. J. Kim, E. D. Jung, J. You, et al., "Perovskites for Next-Generation Colour Conversion Displays," *Nature Electronics* 8 (2025): 886–894, https://doi.org/10.1038/s41928-025-01456-5.

5. S. X. Tao, X. Cao, and P. A. Bobbert, "Accurate and Efficient Band Gap Predictions of Metal Halide Perovskites Using the DFT-1/2 Method: GW Accuracy With DFT Expense," *Scientific Reports* 7, no. 1 (2017): 14386, https://doi.org/10.1038/s41598-017-14435-4.

6. M. Baranowski and P. Plochocka, "Excitons in Metal-Halide Perovskites," *Advanced Energy Materials* 10, no. 26 (2020): 1903659, https://doi.org/10.1002/aenm.201903659.

7. M. Bokdam, T. Sander, A. Stroppa, et al., "Role of Polar Phonons in the Photo Excited State of Metal Halide Perovskites," *Scientific Reports* 6, no. 1 (2016): 28618, https://doi.org/10.1038/srep28618.

8. S. D. Stranks, G. E. Eperon, G. Grancini, et al., "Electron-Hole Diffusion Lengths Exceeding 1 Micrometer in an Organometal Trihalide Perovskite Absorber," *Science* 342, no. 6156 (2013): 341–344, https://doi.org/10.1126/science.1243982.

9. M. Delor, A. H. Slavney, N. R. Wolf, et al., "Carrier Diffusion Lengths Exceeding 1 μm Despite Trap-Limited Transport in Halide Double Perovskites," *ACS Energy Letters* 5, no. 5 (2020): 1337–1345, https://doi.org/10.1021/acsenergylett.0c00414.

10. O. Er-raji, C. Messmer, R. R. Pradhan, et al., "Electron Accumulation across the Perovskite Layer Enhances Tandem Solar Cells With Textured Silicon," *Science* 390, no. 6772 (2025): adx1745, https://doi.org/10.1126/science.adx1745.

11. L. Kong, Y. Sun, B. Zhao, et al., "Fabrication of Red-Emitting Perovskite LEDs by Stabilizing Their Octahedral Structure," *Nature* 631, no. 8019 (2024): 73–79, https://doi.org/10.1038/s41586-024-07531-9.

12. M. Zhang, X. Ma, J. L. Esguerra, et al., "Towards Sustainable Perovskite Light-Emitting Diodes," *Nature Sustainability* 8, no. 3 (2025): 315–324, https://doi.org/10.1038/s41893-024-01503-7.

13. S. Tsarev, D. Proniakova, X. Liu, et al., "Vertically Stacked Monolithic Perovskite Colour Photodetectors," *Nature* 642, no. 8068 (2025): 592–598, https://doi.org/10.1038/s41586-025-09062-3.

14. G. Li, Y. Wang, L. Huang, and W. Sun, "Research Progress of High-Sensitivity Perovskite Photodetectors: A Review of Photodetectors: Noise, Structure, and Materials," *ACS Applied Electronic Materials* 4, no. 4 (2022): 1485–1505, https://doi.org/10.1021/acsaelm.1c01349.

2365709x, 0, Downloaded from https://advanced.onlinelibrary.wiley.com/doi/10.1002/admt.71346 by Universitatsbibliothek RWTH Aachen University, Wiley Online Library on [06/10/2026]. See the Terms and Conditions (https://onlinelibrary.wiley.com/terms-and-conditions) on Wiley Online Library for rules of use; OA articles are governed by the applicable Creative Commons License

15. C. Zou, Z. Ren, K. Hui, et al., "Electrically Driven Lasing From a Dual-Cavity Perovskite Device," *Nature* 645, no. 8080 (2025): 369–374, https://doi.org/10.1038/s41586-025-09457-2.

16. Y. Shi, X. Deng, Y. Gan, L. Xu, Q. Zhang, and Q. Xiong, "Ten Years of Perovskite Lasers," *Advanced Materials* 37, no. 25 (2025): 2413559, https://doi.org/10.1002/adma.202413559.

17. C. Yang, W. Hu, J. Liu, et al., "Achievements, Challenges, and Future Prospects for Industrialization of Perovskite Solar Cells," *Light: Science & Applications* 13, no. 1 (2024): 227, https://doi.org/10.1038/s41377-024-01461-x.

18. K. P. Goetz and Y. Vaynzof, "The Challenge of Making the Same Device Twice in Perovskite Photovoltaics," *ACS Energy Letters* 7, no. 5 (2022): 1750–1757, https://doi.org/10.1021/acsenergylett.2c00463.

19. J. W. Han, S. H. Hwang, M. J. Seol, and S. Y. Kim, "Recent Patterning Methods for Halide Perovskite Nanoparticles," *Advanced Optical Materials* 10, no. 16 (2022): 2200534, https://doi.org/10.1002/adom.202200534.

20. F. Fabrizi, S. Goudarzi, S. Khan, et al., "A Versatile Top-Down Patterning Technique for Perovskite On-Chip Integration," *ACS Nano* 19, no. 33 (2025): 30428–30440, https://doi.org/10.1021/acsnano.5c10397.

21. X. Y. Chin, D. Cortecchia, J. Yin, A. Bruno, and C. Soci, "Lead Iodide Perovskite Light-Emitting Field-Effect Transistor," *Nature Communications* 6, no. 1 (2015): 7383, https://doi.org/10.1038/ncomms8383.

22. J. Mendoza-Carreño, P. Molet, C. Otero-Martínez, M. I. Alonso, L. Polavarapu, and A. Mihi, "Nanoimprinted 2D-Chiral Perovskite Nanocrystal Metasurfaces for Circularly Polarized Photoluminescence," *Advanced Materials* 35, no. 15 (2023): 2210477, https://doi.org/10.1002/adma.202210477.

23. M. A. Gokul and A. Rahman, "Fabrication of High-Performance Devices on Water-Soluble Lead Halide Perovskites Using Water-Based Photolithography," *Advanced Materials Interfaces* 10, no. 6 (2023): 2201749, https://doi.org/10.1002/admi.202201749.

24. J. I. Kwon, G. Park, G. H. Lee, et al., "Ultrahigh-Resolution Full-Color Perovskite Nanocrystal Patterning for Ultrathin Skin-Attachable Displays," *Science Advances* 8, no. 43 (2022): add0697, https://doi.org/10.1126/sciadv.add0697.

25. K. J. Prince, C. P. Muzzillo, M. Mirzokarimov, C. A. Wolden, and L. M. Wheeler, "All-Back-Contact Perovskite Solar Cells Using Cracked Film Lithography," *ACS Applied Energy Materials* 5, no. 8 (2022): 9273–9279, https://doi.org/10.1021/acsaem.2c01298.

26. Z. Gou, S. Huanglong, W. Ke, et al., "Self-Powered X-Ray Detector Based on all-Inorganic Perovskite Thick Film With High Sensitivity Under Low Dose Rate," *physica status solidi (RRL)—Rapid Research Letters* 13, no. 8 (2019): 1900094, https://doi.org/10.1002/pssr.201900094.

27. D. Ahn, M. Lee, Y. Jang, G. Y. Jung, and Y. Pak, "Submicron Patterning Techniques for Perovskite Optoelectronics From Materials Challenges to Scalable Device Integration," *Advanced Optical Materials* 14, no. 6 (2026): 02624, https://doi.org/10.1002/adom.202502624.

28. D. Xu, Q. Wan, S. Wu, et al., "Enhancing the Performance of LARP-Synthesized $CsPbBr_3$ Nanocrystal LEDs by Employing a Dual Hole Injection Layer," *RSC Advances* 10, no. 30 (2020): 17653–17659, https://doi.org/10.1039/D0RA02622K.

29. L. Yang, D. Li, C. Wang, W. Yao, H. Wang, and K. Huang, "Room-Temperature Synthesis of Pure Perovskite-Related Cs_4PbBr_6 Nanocrystals and Their Ligand-Mediated Evolution Into Highly Luminescent $CsPbBr_3$ Nanosheets," *Journal of Nanoparticle Research* 19, no. 7 (2017): 258, https://doi.org/10.1007/s11051-017-3959-7.

30. A. L. Pellegrino and G. Malandrino, "Surfactant-Free Synthesis of the Full Inorganic Perovskite $CsPbBr_3$: Evolution and Phase Stability of $CsPbBr_3$ vs $CsPb_2Br_5$ and Their Photocatalytic Properties," *ACS Applied Energy Materials* 4, no. 9 (2021): 9431–9439, https://doi.org/10.1021/acsaem.1c01636.

31. X. Tang, S. Han, Z. Zu, et al., "All-Inorganic Perovskite $CsPb_2Br_5$ Microsheets for Photodetector Application," *Frontiers in Physics* 5 (2018): 69, https://doi.org/10.3389/fphy.2017.00069.

32. N. Pourdavoud, T. Haeger, A. Mayer, et al., "Room-Temperature Stimulated Emission and Lasing in Recrystallized Cesium Lead Bromide Perovskite Thin Films," *Advanced Materials* 31, no. 39 (2019): 1903717, https://doi.org/10.1002/adma.201903717.

33. G. Tong, T. Chen, H. Li, et al., "Phase Transition Induced Recrystallization and Low Surface Potential Barrier Leading to 10.91%-Efficient CsPbBr3 Perovskite Solar Cells," *Nano Energy* 65 (2019): 104015, https://doi.org/10.1016/j.nanoen.2019.104015.

34. L. Yang, N. Zhang, S. Li, H. Liu, X. Zhang, and Y.-Y. Yu, "Synergistic Top-Down Etching Coupled With In Situ Phase Transition: A Strategy for High-Precision Photolithographic Patterning of Perovskite Single Crystals," *Science China Materials* 69, no. 6 (2026): 3231–3238, https://doi.org/10.1007/s40843-025-3893-y.

35. T. Guoqing, C. Taotao, L. Huan, et al., "Phase Transition Induced Recrystallization and Low Surface Potential Barrier Leading to 10.91%-Efficient $CsPbBr_3$ Perovskite Solar Cells," *Nano Energy* 65 (2019): 104015, https://doi.org/10.1016/j.nanoen.2019.104015.

36. A. D. Wright, C. Verdi, R. L. Milot, et al., "Electron–Phonon Coupling in Hybrid Lead Halide Perovskites," *Nature Communications* 7 (2016): 11755, https://doi.org/10.1038/ncomms11755.

37. Z. Xianzhong and Z. Ziyang, "Electron–Phonon Coupling in $CsPbBr_3$," *AIP Advances* 10, no. 12 (2020): 125015, https://doi.org/10.1063/5.0017149.

Supporting Information

Additional supporting information can be found online in the Supporting Information section.

Supporting File: admt71346-sup-0001-SuppMat.docx.

2365709x, 0, Downloaded from https://advanced.onlinelibrary.wiley.com/doi/10.1002/admt.71346 by Universitatsbibliothek RWTH Aachen University, Wiley Online Library on [06/10/2026]. See the Terms and Conditions (https://onlinelibrary.wiley.com/terms-and-conditions) on Wiley Online Library for rules of use; OA articles are governed by the applicable Creative Commons License